Cellular/Molecular

Trapping of Nicotinic Acetylcholine Receptor Ligands Assayed by *In Vitro* Cellular Studies and *In Vivo* PET Imaging

Hannah J. Zhang,[1*] Matthew Zammit,[1*] Chien-Min Kao,[1*] Anitha P. Govind,[2*] Samuel Mitchell,[1] Nathanial Holderman,[1] Mohammed Bhuiyan,[1] Richard Freifelder,[1] Anna Kucharski,[1] Xiaoxi Zhuang,[2] Jogeshwar Mukherjee,[3†] Chin-Tu Chen,[1†] and William N. Green[2,4†]

[1]Department of Radiology, University of Chicago, Chicago, Illinois 60637, [2]Department of Neurobiology, University of Chicago, Chicago, Illinois 60637, [3]Departments of Preclinical Imaging and Radiological Sciences, University of California, Irvine, California 92697, and [4]Marine Biological Laboratory, Woods Hole, Massachusetts 02543

A question relevant to nicotine addiction is how nicotine and other nicotinic receptor membrane-permeant ligands, such as the anti-smoking drug varenicline (Chantix), distribute in brain. Ligands, like varenicline, with high pK_a and high affinity for α4β2-type nicotinic receptors (α4β2Rs) are trapped in intracellular acidic vesicles containing α4β2Rs *in vitro*. Nicotine, with lower pK_a and α4β2R affinity, is not trapped. Here, we extend our results by imaging nicotinic PET ligands *in vivo* in male and female mouse brain and identifying the trapping brain organelle *in vitro* as Golgi satellites (GSats). Two PET ^{18}F-labeled imaging ligands were chosen: [^{18}F]2-FA85380 (2-FA) with varenicline-like pK_a and affinity and [^{18}F]Nifene with nicotine-like pK_a and affinity. [^{18}F]2-FA PET-imaging kinetics were very slow consistent with 2-FA trapping in α4β2R-containing GSats. In contrast, [^{18}F]Nifene kinetics were rapid, consistent with its binding to α4β2Rs but no trapping. Specific [^{18}F]2-FA and [^{18}F]Nifene signals were eliminated in β2 subunit knock-out (KO) mice or by acute nicotine (AN) injections demonstrating binding to sites on β2-containing receptors. Chloroquine (CQ), which dissipates GSat pH gradients, reduced [^{18}F]2-FA distributions while having little effect on [^{18}F]Nifene distributions *in vivo* consistent with only [^{18}F]2-FA trapping in GSats. These results are further supported by *in vitro* findings where dissipation of GSat pH gradients blocks 2-FA trapping in GSats without affecting Nifene. By combining *in vitro* and *in vivo* imaging, we mapped both the brain-wide and subcellular distributions of weak-base nicotinic receptor ligands. We conclude that ligands, such as varenicline, are trapped in neurons in α4β2R-containing GSats, which results in very slow release long after nicotine is gone after smoking.

Key words: addiction; fluorescence; mouse model; nicotine; positron emission tomography; smoking cessation

Significance Statement

Mechanisms of nicotine addiction remain poorly understood. An earlier study using *in vitro* methods found that the anti-smoking nicotinic ligand, varenicline (Chantix) was trapped in $\alpha4\beta2$R-containing acidic vesicles. Using a fluorescent-labeled high-affinity nicotinic ligand, this study provided evidence that these intracellular acidic vesicles were $\alpha4\beta2$R-containing Golgi satellites (GSats). *In vivo* PET imaging with F-18-labeled nicotinic ligands provided additional evidence that differences in PET ligand trapping in acidic vesicles were the cause of differences in PET ligand kinetics and subcellular distributions. These findings combining *in vitro* and *in vivo* imaging revealed new mechanistic insights into the kinetics of weak base PET imaging ligands and the subcellular mechanisms underlying nicotine addiction.

Received Dec. 17, 2021; revised Aug. 7, 2022; accepted Aug. 13, 2022.

Author contributions: M.Z. edited the paper; X.Z., J.M., C.-T.C., and W.N.G. designed research; H.J.Z., M.Z., C.-M.K., A.P.G., S.M., N.H., M.B., R.F., A.K., J.M., C.-T.C., and W.N.G. performed research; H.J.Z., M.Z., C.-M.K., A.P.G., S.M., N.H., J.M., C.-T.C., and W.N.G. analyzed data; H.J.Z., M.Z., C.-M.K., A.P.G., J.M., C.-T.C., and W.N.G. wrote the paper.

This work was supported in part by National Institutes of Health (NIH) Grants R01 DA044760-01 (to J.M., C.-T.C. and W.N.G.), RF1 AG029479 (to J.M.), and T32 DA043469 (to M.Z.). The authors acknowledge the assistance from the Integrative Small Animal Imaging Research Resources (iSAIRR) supported in part by NIH Grants P30 CA14500 and S10 OD025265 and from the Cyclotron Facility of the University of Chicago.

*H.J.Z, M.Z., C.-M.K., and A.P.G. contributed equally to this work.

†J.M., C.-T.C., and W.N.G. equally supervised this work.

The authors declare no competing financial interests.

Correspondence should be addressed to Chin-Tu Chen at c-chen@uchicago.edu or William N. Green at wgreen@uchicago.edu.

https://doi.org/10.1523/JNEUROSCI.2484-21.2022

Introduction

Tobacco use continues world-wide and is the leading cause of preventable deaths in the United States [National Center for Chronic Disease Prevention and Health Promotion (US) Office on Smoking and Health, 2014]. Nicotine, the addictive molecule in tobacco, binds to high-affinity nicotinic acetylcholine receptors (nAChRs) in the brain, where it initiates its addictive effects. nAChRs are members of the Cys-loop family of ligand-gated ion channels, all of which are pentameric neurotransmitter receptors (Karlin, 2002; Albuquerque et al., 2009). In mammalian brains, high-affinity nicotine binding sites are largely nAChRs containing $\alpha4$ and $\beta2$ subunits ($\alpha4\beta2$Rs; Albuquerque et al., 2009). In

mice, knock-out (KO) of either subunit reduced the pharmacological and behavioral effects of nicotine (Picciotto et al., 1998; Marubio et al., 2003), and this effect can be rescued by targeted $\beta2$ subunit expression in the mid-brain reward ventral tegmental area (VTA; Maskos et al., 2005).

Chronic nicotine exposure causes $\alpha4\beta2$R upregulation, a complex set of long-term changes causing both increases in $\alpha4\beta2$R high-affinity binding site numbers and functional upregulation, the increased $\alpha4\beta2$R functional response after nicotine exposure (Marks et al., 1983; Schwartz and Kellar, 1983; Benwell et al., 1988; Breese et al., 1997). Several other studies link the process of nicotine-induced $\alpha4\beta2$R upregulation to nicotine addiction (Vezina et al., 2007; Govind et al., 2009, 2012; Lewis and Picciotto, 2013). Nicotine and other weak-base ligands of $\alpha4\beta2$Rs, unlike acetylcholine, are highly membrane-permeant and rapidly reach equilibrium in intracellular organelles and concentrate in acidic organelles (Brown and Garthwaite, 1979). The anti-smoking drug, varenicline (Chantix), is selectively trapped as a weak base within intracellular acidic vesicles that contain high-affinity $\alpha4\beta2$Rs because of its high pK_a and binding-affinity (Govind et al., 2017). Nicotine, with lower pK_a and affinity, is not trapped but concentrates in vesicles. Nicotine upregulation amplifies varenicline trapping by increasing the number of high-affinity binding sites, which increases the capacity of the acidic vesicles to trap varenicline and increasing acidic vesicle numbers.

Nicotine and varenicline bind to the same site on $\alpha4\beta2$Rs in the brain. However, their residence times and kinetics in the brains of smokers are regulated by their trapping in $\alpha4\beta2$R-containing acidic vesicles. Because nicotine is not trapped, its residence time in brain is 1–2 h while varenicline, which is trapped, has a residence time of 4–5 d. Our findings suggested that varenicline trapping in $\alpha4\beta2$R-containing acidic vesicles may play a significant role in its smoking cessation actions by maintaining varenicline concentrations in the brain selectively in neurons where $\alpha4\beta2$Rs are expressed. We found *in vitro* that trapped varenicline is slowly released and acts to desensitize $\alpha4\beta2$Rs that had been functionally upregulated by prior nicotine exposure (Govind et al., 2017). If a similar effect of slowly released varenicline occurs in vivo and desensitizes functionally upregulated $\alpha4\beta2$Rs, varenicline acts to reduce the initial smoker craving that drives the return to smoking each day. Together, our findings suggest novel mechanisms underlying smoking cessation and new strategies for therapeutic development.

Here, we address whether the distribution of PET tracers used to assay $\alpha4\beta2$Rs *in vivo*, which are weak bases, are affected by trapping in $\alpha4\beta2$R-containing acidic vesicles. Because of the limits of PET image resolution, we performed *in vitro* cell binding competition assays to assess ligand trapping, which allow subcellular resolution using the same PET ligands. We present evidence that 2-FA85380 (2-FA) used as a PET tracer is trapped in $\alpha4\beta2$R-containing acidic vesicles similar to varenicline trapping while Nifene is largely not trapped similar to nicotine. The identity of $\alpha4\beta2$R-containing acidic vesicles is unknown. Recently, we found that a novel intracellular compartment in neurons, Golgi satellites (GSats), contain high levels of $\alpha4\beta2$Rs and GSat numbers are increased by nicotine exposure as well as increased neuronal activity (Govind et al., 2021). Using a fluorescent-tagged $\alpha4\beta2$R ligand, Nifrorhodamine, to image the subcellular localization of $\alpha4\beta2$Rs, we present evidence that $\alpha4\beta2$Rs accumulate in acidic vesicles that are GSats. Live PET imaging in mice using [^{18}F]Nifene and [^{18}F]2-FA were consistent with *in vitro* results with the kinetics of [^{18}F]2-FA PET signals were much slower than that of [^{18}F]Nifene consistent with [^{18}F]2-FA being trapped in acidic vesicles. Chloroquine (CQ), which dissipates the pH gradient across acidic organelles, reduced trapping *in vitro* and reduced [^{18}F]2-FA's distribution volume ratios (DVRs) in midbrain and thalamus while having little to no effect on [^{18}F]Nifene DVR values. Altogether, we conclude that 2-FA is trapped and images $\alpha4\beta2$Rs in GSats while Nifene images all ligand-binding $\alpha4\beta2$Rs because it is not confined to GSats.

Material and Methods

Cellular binding competition assay

HEK cells stably expressing $\alpha4\beta2$Rs were treated with 10 μM nicotine overnight. Cells were then washed four times with PBS, scraped off the plates, and suspended in PBS. Aliquots of cells were incubated with indicated concentrations of 2-FA, Nifene or nicotine respectively for 5 min followed by addition of 2.5 nM [^{125}I]-epibatidine ([^{125}I]-Epb; 2200 Ci/mmol; PerkinElmer) and incubation for 20 min at room temperature. At the end of incubation, cells were harvested on Whatman GF/B filters presoaked in 0.5% polyethyleneimine and washed four times with PBS using a 24-channel cell harvester (Brandel). Nonspecific binding was estimated by incubating parallel samples in 1 mM nicotine with [^{125}I]Epb. Radioactivity of bound [^{125}I]Epb was determined using a γ counter (Wallac, PerkinElmer). The binding of [^{125}I]Epb was normalized to the binding of cells without 2-FA, Nifene or nicotine treatment and plotted as percent of untreated cells.

Mammalian cell culture

Stable cell lines expressing rat $\alpha4\beta2$ nAChRs in HEK cells are from our lab, expressing untagged $\alpha4$ and C-terminal, HA epitope-tagged $\beta2$ subunits (Vallejo et al., 2005). Cell lines were maintained in DMEM (Invitrogen, Life Technologies) with 10% calf serum (Hyclone, GE Healthcare Life Sciences) at 37°C in the presence of 5% CO_2. DMEM was supplemented with Hygromycin (Thermofisher Scientific) at 0.4 mg/ml for maintaining selection of $\alpha4\beta2$ HEK cells. Stable cells were plated in media without hygromycin for experiments.

Primary neuronal culture and transfections

Primary cultures of rat cortical neurons were prepared as described (Govind et al., 2012) using Neurobasal Media (NBM), 2% (v/v) B27, and 2 mM L-glutamine (all from Thermofisher Scientific). Dissociated cortical cells from E18 Sprague Dawley rat pups were plated on slips or plates coated with poly-D-lysine. For live imaging, neurons were plated in 35 mm glass bottom dishes (MatTek). Cells were plated at a density of 0.25×10^6 cells/ml on 35-mm dishes or per well in a six-well plate. Neuronal cultures were transfected at days in vitro (DIV) 10 with the Lipofectamine 2000 transfection reagent (Thermofisher Scientific) according to manufacturer's recommendations. Neurons were transfected with cDNAs of $\alpha4$, $\beta2_{HA}$ and Golgi markers, St3 GFP or St3 Halo. 0.5 μg of each DNA up to a total of 1.5 μg were used per 35-mm imaging dish or per well of a six-well plate; 24 h after transfection, neurons were treated with 1 μM nicotine for 17 h.

Ligand treatment and ^{125}I-epibatidine binding

$\alpha4\beta2$R HEK cells were treated with 10 μM nicotine, 100 μM Nifene, or 100 μM 2-FA for 17 h at 37°C in medium. Information for each ligand is displayed in Table 1. Cells were washed four times with PBS and collected by scraping off from the plates using a cell scraper with PBS, resuspended in 1 ml PBS. 1/20th of the cell suspension was distributed to three tubes followed by incubation

Table 1. Nicotinic ligand acidity and affinity for $\alpha4\beta2$ receptors

Compound	Ki	pK_a	Log P	Source
Nicotine	5.45 nM (human)[a]	8[c,d]	1.17[e]	a. Mukherjee et al. (2018)
	1.68 nM (rat)[b]			b. Pichika et al. (2006)
	0.94 nM[c]			c. This work
Nifene	0.83 nM (human)[a]	9.19[c]	−0.52[b]	d. Lu et al. (2007)
	0.50 nM (rat)[b]			e. Hansch and Leo (1995)
	0.31 nM[c]			f. Valette et al. (1999)
2-FA85380	0.08 nM[f]	10.5[c,d]	−2.09[h]	g. Gao et al. (2008)
	1.33 nM[g]			h. Brown et al. (2004)
	0.07 nM[c]			i. Davila-Garcia et al. (1997)
Iodoepibatidine	0.09 nM[i]	10.5[k]	NA	j. Govind et al. (2017)
	0.01–0.05 nM[j]			k. Thompson et al. (2017)
Varenicline	0.4 nM[j]	9.2[j]	−0.82	

in 2.5 nM [^{125}I]-Epb for 15 min. For competition experiments, intact cells were preincubated in the indicated concentrations of Nifene, 2-FA or nicotine for 5 min, followed by the addition of 2.5 nM [^{125}I]-Epb for 15 min. All binding was terminated by vacuum filtration through Whatman GF/B filters presoaked in 0.5% polyethyleneimine using a Brandel 24-channel cell harvester. Bound [^{125}I]-Epb (2200 Ci/mmol) was determined by γ counting (PerkinElmer Wallac) with nonspecific binding estimated by [^{125}I]-Epb binding to cells that were preincubated with 1 mM nicotine before epibatidine binding.

Altering intracellular pH of acidic intracellular organelles

Intact cells were treated with nAChR ligands for 17 h and washed twice with PBS. Cells were exposed to two 5-min incubations with PBS containing 15, 150 μM CQ or 20 mM NH_4Cl to neutralize the pH of intracellular organelles and washed two times with PBS. Cells were gently scraped from the plates, re-suspended in PBS, and subjected to [^{125}I]-Epb binding as described above.

Immunocytochemistry

Live labeling experiments were performed on cultured neurons grown in imaging chambers (MaTek), transfected with nAChR subunits $\alpha4$ and $\beta2$ and Golgi markers, St3-GFP or St3-Halo for 24 h and treated with 1 μM nicotine for 17 h. Neurons were labeled with 25 μM Nifrorhodamine (analog of Nifrofam; Samra et al., 2018) or pHRodo (Thermofisher) as per manufacturers instruction for 30 min, washed three times with low fluorescence Hibernate E buffer (Brain Bits) and imaged live in the same buffer. For total $\beta2$ staining, neurons were grown on coverslips, fixed with 4% paraformaldehyde + 4% sucrose for 10 min and permeabilized with 0.1% Triton X-100. $\beta2$ subunits were imaged using monoclonal anti-$\beta2$ antibody, mAb12H and fluorescent secondary antibody, previously validated (Walsh et al., 2018), which gave results very similar to using mouse anti-HA antibody (Govind et al., 2021). Primary antibody incubations were for 1 h and secondary antibodies for 45 min unless otherwise mentioned. Coverslips were mounted using Prolong Gold mounting media with DAPI. Fluorescence images were acquired using a Marianas Yokogawa type spinning disk confocal microscope with back-thinned EMCCD camera. Images were processed and analyzed using ImageJ/Fiji (NIH).

Animals

The male and female $\beta2$ nAChR KO mice and their wild-type (WT) littermates were generated in house by breeding a heterozygous pair on the C57BL/6J background purchased from The Jackson Laboratory (Picciotto et al., 1995). Additional male and female WT mice at the same age were purchased directly from the Jackson lab and used in the same manner as the WT littermates. Animals were housed in The University of Chicago Animal Research Resources Center. The Institutional Animal Care and Use Committee of the University of Chicago, in accordance with National Institutes of Health guidelines, approved all animal procedures. Mice were maintained at 22–24°C on a 12/12 h light/dark cycle and provided food (standard mouse chow) and water *ad libitum*. Mice aged between 3 and 10 months were used in this study. The number of the animals and their body weights (BWs) are summarized in Table 2.

Acute nicotine (AN) supplement

To demonstrate the binding specificity of weak base ligands, AN administration was performed to a group of WT mice. Nicotine ditartarte (Sigma-Aldrich) was prepared in isotonic saline at the concentration of 0.1 mg/ml freshly and filtered through a 0.2 μm syringe filter. Each mouse was injected 0.5 mg/kg BW of nicotine intraperitoneally 15 min before the tracer administration and PET imaging according to the imaging protocol describe in the following sections.

CQ treatment

Chloroquine diphosphate (CQ; Sigma-Aldrich) was dissolved in PBS and filtered through a 0.2-μm syringe filter. WT mice were used in the CQ treatment group (CQWT). Each mouse received 50 mg/kg BW/d of CQ by intraperitoneal injection for 3 d (Vodicka et al., 2014). 10 min after the third CQ injection, animals underwent [^{18}F]2-FA or [^{18}F]Nifene administration and PET imaging according to the imaging protocol described in following sections.

Radiotracer syntheses

Syntheses of both [^{18}F]2-FA and [^{18}F]Nifene, two radiotracers for $\alpha4\beta2$Rs, were conducted at the Cyclotron Facility of The University of Chicago. [^{18}F]2-FA was synthesized from the commercially available precursor, 2-TMA-A85380. The [^{18}F]Nifene was synthesized from the precursor N-BOC-nitroNifene. An IBA Synthera V2 automatic synthesis module equipped with Synthera preparative HPLC was used for the radiolabeling and purification inside a Comecer hot cell. Typical yield for [^{18}F]2-FA was 34% (decay corrected) with specific activities >3000 mCi/μmol and radiochemical purity >99%. The representative radiochemical yield was 6.3% (decay corrected) with specific activities >3000 mCi/μmol and >99% purity for [^{18}F]Nifene.

PET/CT imaging

The imaging protocols were designed based on previous reports for [^{18}F]2-FA and [^{18}F]Nifene (Horti et al., 2000; Pichika et al., 2006; Constantinescu et al., 2013) and our preliminary experiments fine-tuning the protocol (data not shown). An intraperitoneal catheter was placed at the lower right abdominal area of each mouse before the imaging. The animal was then placed into the β-Cube preclinical microPET imaging system (Molecubes) in a small animal holder. The tracer was delivered in 200-μl isotonic saline via the IP catheter at the same time when the PET imaging starts and followed by flushing 100 μl of fresh saline. The injected doses were summarized in Table 2. Whole-body imaging was acquired with 133 × 72 mm field of view (FOV) and an average spatial resolution of 1.1 mm at the center of FOV (Krishnamoorthy et al., 2018). List-mode data were recorded for 3 h for [^{18}F]2-FA and 1 h for [^{18}F]Nifene followed by a reference

Table 2. Baseline information of the animals imaged with PET

		WT	KO	AN	CQ
Sample, *n*	2-[^{18}F]-2-A85380	10	11	10	6
	[^{18}F]-Nifene	12	7	4	8
BW, g	Male	30.5 ± 0.6	30.6 ± 0.8	27.2 ± 2.2	29.9 ± 0.8
	Female	21.6 ± 0.7	21.0 ± 0.5	18.8 ± 0.8	22.1 ± 0.4
Injected dose of 2-[^{18}F]-2-A85380 (μCi)		192 ± 13	149 ± 13	201 ± 11	137 ± 7
Injected dose of [^{18}F]-Nifene (μCi)		126 ± 7	87 ± 13	152 ± 2	146 ± 5

CT image on the X-Cube preclinical microCT imaging system (Molecubes). The images were reconstructed using an OSEM reconstruction algorithm that corrected for attenuation, randoms and scatter with an isotropic voxel size of 400 μm and a rebinned frame rate of 18 × 10 min for [^{18}F]2-FA and 6 × 10 min for [^{18}F]Nifene. CT images were reconstructed with a 200-μm isotropic voxel size and used for anatomic co-registration, scatter correction and attenuation correction. Animals were maintained under 1–2% isoflurane anesthesia in oxygen during imaging. Respiration and temperature were constantly monitored and maintained using the Molecubes monitoring interface, and Small Animal Instruments (SAII Inc) set up. All animals survived the imaging.

Data analyses of tracer uptake

To quantify the brain tracer uptake, analyses of CT-fused PET images were performed using VivoQuant software (Invicro). Dynamic tracer uptake was analyzed and expressed in standardized uptake values (SUVs) in multiple 10-min frames to generate time active curves (TACs; Keyes, 1995; Huang, 2000; Hesterman et al., 2019):

$$\mathrm{SUV} = \frac{\text{radioactivity concentration in volume of interest (VOI)}\left(\frac{\mu\mathrm{Ci}}{\mathrm{ml}}\right)}{\frac{\text{injected dose}\ (\mu\mathrm{Ci})}{\text{body weight of animal}\ (\mathrm{g})}}.$$

Brain regional analysis was performed using a 3D mouse brain atlas available as a VivoQuant software plug-in. The 3D brain atlas is based on the Paxinos–Franklin atlas registered to a series of high-resolution magnetic resonance images with 100 μm near isotropic data and has been applied in other studies (Slavine et al., 2017; Hesterman et al., 2019; Mazur et al., 2019). The brain was segmented into 14 regions within the skull of each animal using the CT as the reference for automatic registration. Among the 14 regions, six regions (cerebellum, cortex, hippocampus, midbrain, striatum, and thalamus) that represent the high, middle and low nicotinic receptor levels in the brain are presented in this study. Because of the small size of some brain regions (e.g., hippocampus), partial volume effects and activity spillover from neighboring regions may lead to some under or over estimation of radiotracer when using the software to extract the volumes-of-interest (VOI). The VOI of the whole brain was 473 ± 3.39 mm^3 (mean ± SEM).

DVR calculation

PMOD kinetic modeling software (Bruker) was used to compute the DVR of the thalamus and midbrain of each mouse using Logan graphical analysis (Logan et al., 1996) with the cerebellum used as the reference region. Using the concentration TACs generated from the VOIs from the VivoQuant brain atlas, a simplified reference tissue model (SRTM) was used to compute the k_2' value for each region. Then a Logan plot was created, and the slope used as the DVR.

Statistical analyses

Statistical analyses were performed using Prism software (GraphPad). All cellular data and all PET data were normally distributed. Continuous data were summarized as mean with standard errors with statistically significant differences assessed using *t* test between two groups and one-way and two-way ANOVA among multiple groups; $p < 0.05$ was considered statistically significant.

Results

Trapping of α4β2R PET ligands in α4β2R-containing intracellular acidic vesicles

Previously, we have found that the degree to which weak-base α4β2R ligands are trapped is dependent on both their pK$_a$ values and their affinity values for α4β2R binding sites (Govind et al., 2017; for values, see Table 1). In order to estimate α4β2R affinity values for the PET ligands, Nifene and 2-FA (see structure in Fig. 1*A*), we performed competitive binding of the two ligands and nicotine using [^{125}I]-Epb binding to α4β2Rs expressed in HEK cells. The Ki values from the fits to the data (Fig. 1*B*) were 7.1×10^{-11} M for 2-FA, 3.1×10^{-10} M for Nifene and 9.4×10^{-10} M for nicotine indicating that Nifene has a higher affinity for α4β2R binding sites than nicotine, and 2-FA a higher affinity than Nifene. These estimates (Table 1) of 2-FA and Nifene affinities for α4β2R binding sites together with their pK$_a$ values (Hansch and Leo, 1995; Davila-Garcia et al., 1997; Valette et al., 1999; Brown et al., 2004; Pichika et al., 2006; Lu et al., 2007; Gao et al., 2008; Govind et al., 2017; Thompson et al., 2017; Mukherjee et al., 2018) suggest that 2-FA and Nifene could become trapped in α4β2R-containing intracellular acidic vesicles similar to varenicline and epibatidine.

To assay for the trapping of Nifene and 2-FA in α4β2R-containing intracellular acidic vesicles, we performed a different assay that also made use of [^{125}I]-Epb. As described previously (Govind et al., 2017), the assay measures the degree to which a 17-h exposure to the ligand increased the number of high-affinity α4β2R binding sites using [^{125}I]-Epb binding, which is a measure of α4β2R upregulation by the ligand. If the assay is performed on live HEK cells expressing α4β2Rs, varenicline (Fig. 1*C*) and epibatidine (Govind et al., 2017) do not cause any significant upregulation (adjusted $p > 0.05$) compared with the 5-fold upregulation with nicotine exposure (adjusted $p < 0.0001$; Fig. 1*C*). However, if the assay is performed using membranes prepared from the cells in which intracellular acidic vesicles are not intact, α4β2R upregulation by varenicline and epibatidine is similar to that by nicotine (Govind et al., 2017). These data are consistent with varenicline and epibatidine being concentrated and trapped within the α4β2R-containing intracellular acidic

vesicles, thereby preventing [^{125}I]-Epb binding because varenicline and epibatidine are occupying the $\alpha4\beta2$R binding sites in the vesicle lumen. Like varenicline, $\alpha4\beta2$Rs were not upregulated by 2-FA for live HEK cells (adjusted $p > 0.05$; Fig. 1*C*). In contrast, $\alpha4\beta2$Rs were upregulated by Nifene almost to the same degree as upregulation by nicotine (adjusted $p < 0.0001$; Fig. 1*C*). These findings suggest that 2-FA is trapped within $\alpha4\beta2$R-containing intracellular acidic vesicles similar to varenicline while little to no Nifene is trapped.

Upregulation by varenicline and epibatidine could be partially restored for live HEK cells by different treatments that dissipated the pH gradient across the vesicle membrane. These included the addition of a weak base that is not a $\alpha4\beta2$R ligand, CQ or ammonium chloride (NH_4Cl). Consistent with 2-FA trapping within $\alpha4\beta2$R-containing intracellular acidic vesicles, both CQ at 15 or 150 μM and ammonium chloride at 20 mM increased the effects of 2-FA [ANOVA F(df): 118.9(5); adjusted $p < 0.0001$] and varenicline [ANOVA F (df): 187.6(5); adjusted $p < 0.0001$] in terms of the upregulation of $\alpha4\beta2$Rs in the HEK cells (Fig. 1*D*). In contrast, CQ and ammonium chloride, treatments that dissipated the pH gradient across the vesicle membrane, had no effect on upregulation by nicotine and Nifene (adjusted $p > 0.05$) consistent with a lack of trapping (Fig. 1*E*).

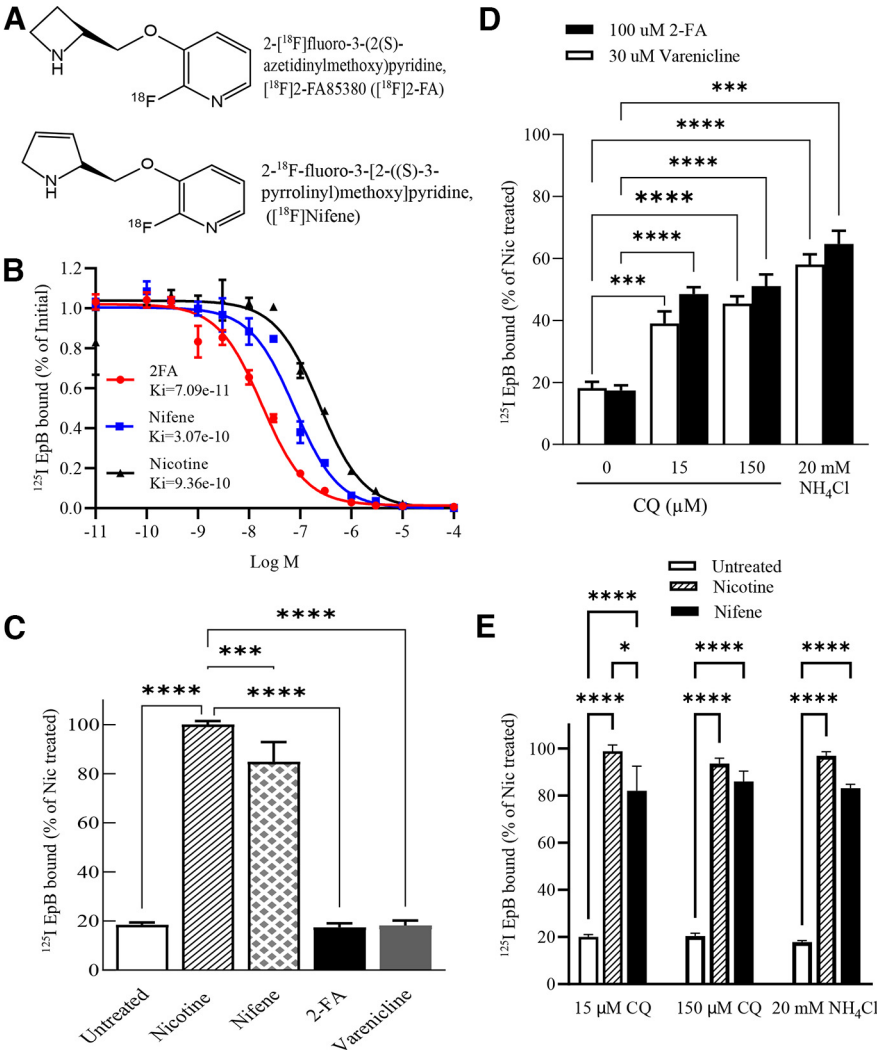

Figure 1. ***A***, Chemical structures of 2-[^{18}F]fluoro-3-(2(S)-azetidinylmethoxy)pyridine and (2-^{18}F-fluoro-3-[2-((S)—3-pyrrolinyl)methoxy]pyridine. ***B***, Competition of the ligands, nicotine (black triangle), Nifene (blue square), or 2-FA (red circle), for high-affinity binding sites on $\alpha4\beta2$Rs as assayed by ^{125}I-epibatidine binding. Live $\alpha4\beta2$R-expressing HEK cells were incubated with the indicated concentrations of nicotine, Nifene, or 2-FA for 5 min before ^{125}I-epibatidine binding. Data are plotted as the fraction of the initial ^{125}I-epibatidine bound to intact cells in the absence any added ligands. Each point is the mean ± SEM. ***C***, Trapping of 2-FA and not Nifene in intact $\alpha4\beta2$R HEK cells. Cells were treated for 17 h with Nicotine (10 μM), Nifene (100 μM), 2-FA (100 μM), or varenicline (30 μM) and ^{125}I-epibatidine binding performed on live cells ($n = 3$). Specific epibatidine binding was represented as % of binding relative to nicotine-treated cells. ***D***, Loss of trapped 2-FA by disrupting intracellular pH gradient. $\alpha4\beta2$R HEK cells were treated with 2-FA and varenicline for 17 h. Cells were either washed with PBS or exposed to agents that raise pH in intact cells like CQ (15 or 150 μM) or NH_4Cl (20 mM) for 10 min. ^{125}I-epibatidine binding was performed and data plotted as in ***C***. Each point is the mean ± SEM, $n = 3$ for 2-FA and $n = 5$ for varenicline. ***E***, Disrupting intracellular pH gradient had no effects on untreated cultures or cultures treated with nicotine or Nifene. $\alpha4\beta2$R HEK cells were untreated or treated with nicotine or Nifene for 17 h and then treated with CQ (15 or 150 μM) or NH_4Cl (20 mM) for 10 min as in ***C***. In all the column graphs in ***C–E***: *$p < 0.05$, **$p < 0.001$, ***$p < 0.0001$, ****$p < 0.00001$ by one-way ANOVA with Bonferroni's multiple comparison test.

Are $\alpha4\beta2$R-containing intracellular acidic vesicles GSats?

We have recently characterized changes in the Golgi apparatus (GA) that occur with nicotine exposure and parallel upregulation of $\alpha4\beta2$Rs (Govind et al., 2021). With nicotine exposure, small organelles, GSats, form out of the endoplasmic reticulum (ER). GSat formation only occurs in response to nicotine when $\alpha4\beta2$Rs are expressed in HEK cells or in neurons and the effects of nicotine are reversible. GSats had not been characterized previously because the usual Golgi markers used to image Golgi are Golgi structural proteins that are not found in GSats (Govind et al., 2021). To examine whether the $\alpha4\beta2$R-containing intracellular acidic vesicles are GSats, we used the Golgi enzyme sialyltransferase Gal3 (St3), which label GSats in addition to the GA.

In Figure 2, we imaged GSats by expressing a GFP-tagged version of St3 in cultured rat cortical neurons together with $\alpha4$ and HA-tagged $\beta2$ subunits. St3-GFP labels the GA found in the soma of untreated neurons (Fig. 2, –Nicotine panels) or neurons that have been exposed to nicotine for 17 h (Fig. 2, +Nicotine panels), which increases the numbers of GSats (Govind et al., 2021). St3-GFP also labels smaller GSat structures that extend out into the neuronal processes. Two different examples of neurons are displayed in Figure 2*A*,*B*, both expressing St3-GFP (green), but with the $\alpha4\beta2$Rs labeled using different probes. In Figure 2*A*, the $\alpha4\beta2$Rs were labeled with fluorescent anti-$\beta2$ antibody that specifically labels all $\beta2$ subunits assembled and unassembled (Walsh et al., 2018), which includes transfected and endogenous subunits. The labeled $\beta2$ subunits are found largely in the ER where $\beta2$ subunits are synthesized and assemble with $\alpha4$ into $\alpha4\beta2$Rs (Sallette et al., 2005). The probe also stains the GA but appears to have little overlap with the smaller St3 puncta, which are the GSats. This apparent lack of overlap results from the very bright staining of the $\beta2$ subunits in the ER relative to $\beta2$ subunit staining of the GSats. The presence of

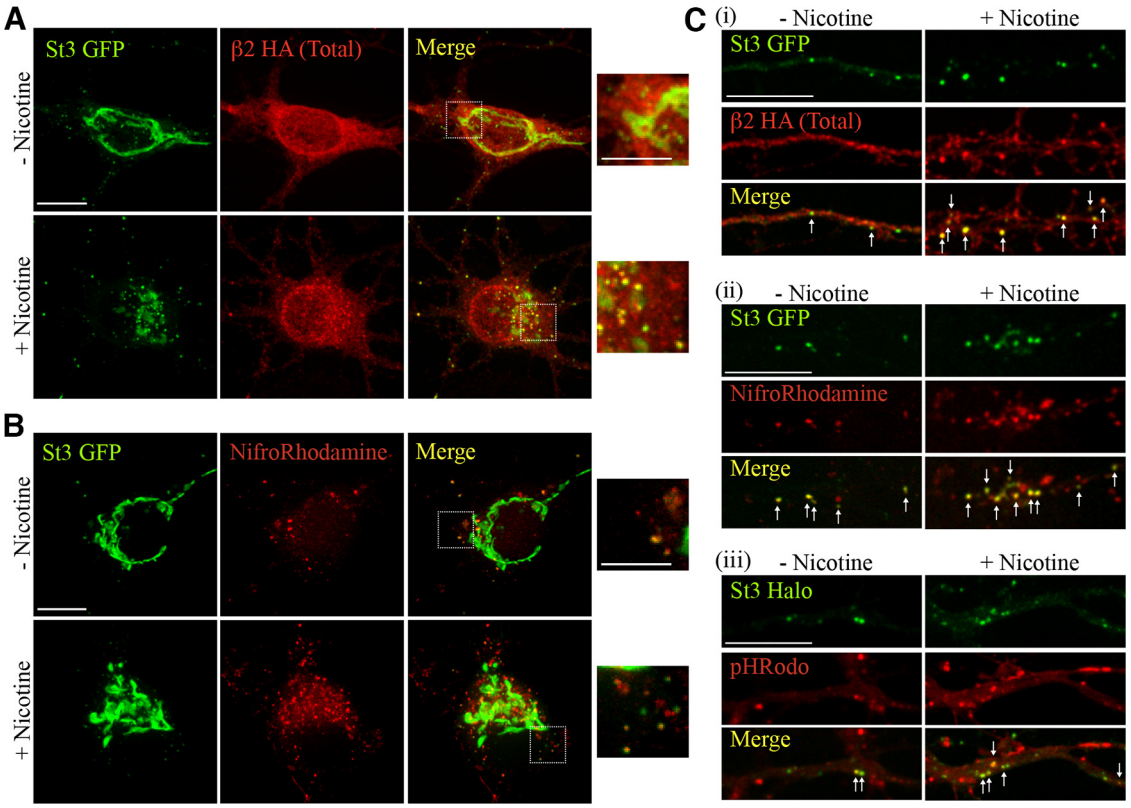

Figure 2. Nifrorhodamine labeling of GSats in primary cortical cultures expressing $\alpha4\beta2$Rs. ***A***, Cultured neurons (DIV 10) were expressing the GSat marker St3-GFP (green) and $\alpha4$ and $\beta2$HA subunits. After 24 h, cultures were treated with 1 μM nicotine for 17 h (+Nicotine) or untreated (–Nicotine). Neurons were fixed, permeabilized and stained for all $\beta2$ subunits with monoclonal anti-$\beta2$ antibody, mAb12H (red; secondary antibody anti-mouse Alexa 568). Scale bar, 10 μm. Inset scale bar, 5 μm. ***B***, High-affinity $\alpha4\beta2$R binding sites were labeled with Nifrorhodamine in primary cortical cultures expressing $\alpha4\beta2$Rs. Cultured neurons were transfected and treated with nicotine as in ***A***. Cultures were labeled with 25 μM Nifrorhodamine (red) for 30 min and imaged live. Scale bar, 10 μm. Inset scale bar, 5 μm. Inset scale bar. ***C***, Dendritic GSats contain high-affinity $\alpha4\beta2$R binding sites and are acidic. ***i***, $\beta2$ subunit labeling of dendrites of neurons expressing St3-GFP (green) and $\alpha4$ and $\beta2$-HA subunits (anti-$\beta2$- mAb12H, red) after permeabilization and fixation as in ***A***. ***ii***, Live labeling of Nifrorhodamine (red) with St3-GFP (green) as in ***B***. ***iii***, Live labeling with pH-sensitive dye, pHrodo (red), with St3-Halo expression (green). Arrows mark GSats with co-labeling for $\beta2$-HA subunits, Nifrorhodamine or pHrodo. Scale bar, 10 μm.

$\beta2$ subunits in GSats is observed when we increase the resolution of the images in the soma (Fig. 2*A*, insets) especially in the +Nicotine image. The $\beta2$ subunit staining of the GSats in even better observed in dendrites (Fig. 2*Ci*) where the levels of ER are much smaller, and consequently, staining of $\beta2$ subunits in ER is much weaker.

In Figure 2*B*, $\alpha4\beta2$Rs were labeled using a membrane-permeable, fluorescently-labeled analog of the 2-FA ligand, Nifrorhodamine, that binds to $\alpha4\beta2$R high-affinity binding sites. In order to obtain a fluorescent probe for $\alpha4\beta2$Rs, significant modification in the structure was necessary because of the lack of functionality of 2-FA and Nifene for fluorophore labeling (for details, see Samra et al., 2018). The modifications necessary to add rhodamine to 2-FA resulted in an analog closer to Nifrolidine, which is a similar $\alpha4\beta2$R ligand used for PET imaging (Chattopadhyay et al., 2005). Surprisingly, Nifrorhodamine labeling does not colocalize with $\beta2$ subunit staining in the ER or GA in the soma. Instead, Nifrorhodamine labeling co-localizes with the GSats labeled with St3-GFP in the soma (Fig. 2*B*) and dendrites (Fig. 2*Cii*). These findings suggest that $\alpha4\beta2$R high-affinity binding sites form in GSats and not during assembly in the endoplasmic reticulum (ER). Shown in the right panels of Figure 2*Ciii* are dendrites expressing St3-GFP and labeled with pHrodo, a fluorescent probe that fluoresces at pH values found in acidic vesicles. pHrodo fluorescence overlays with a significant number of the St3-positive puncta as well as other acidic organelles consistent with mature GSats being acidic vesicles.

PET studies with [^{18}F]2-FA and [^{18}F]Nifene

We measured the binding kinetics of $\alpha4\beta2$R ligands *in vivo*, using [^{18}F]2-FA and [^{18}F]Nifene for brain PET imaging in mice. Figure 3*A* displays typical images of [^{18}F]2-FA and [^{18}F]Nifene binding at coronal, sagittal, and transverse sections of the brain in WT mice. Whole-brain uptake of [^{18}F]Nifene was significantly greater than [^{18}F]2-FA as seen in Figure 3*A*. The TACs of the whole brain from the WT mice for [^{18}F]2-FA and [^{18}F]Nifene are shown in Figure 3*B*; [^{18}F]Nifene demonstrated fast kinetics peaking at ~10 min with a SUV of ~1.6 after tracer injection. In contrast the binding of [^{18}F]2-FA was slower peaking at ~50 min with a SUV of ~0.6. The significant difference in brain kinetics between the two radiotracers is seen in Figure 3*B*, inset, where whole-brain [^{18}F]Nifene reduces to below 50% levels within 40 min, whereas [^{18}F]2-FA remained at ~70% of the peak at the end of 3-h imaging time.

The whole-brain retention for both [^{18}F]2-FA and [^{18}F]Nifene was significantly decreased in the $\beta2$ KO mice. This is similar to our previous observations of a lack of [^{18}F]Nifene binding in $\beta2$ KO mice (Bieszczad et al., 2012). Similarly, [^{18}F]2-FA cleared from the $\beta2$ KO mice brain more rapidly, with SUV values reduced by ~50% of WT animals at 3 h after injection (Fig. 3*C*). Reductions in whole-brain SUVs of [^{18}F]Nifene were

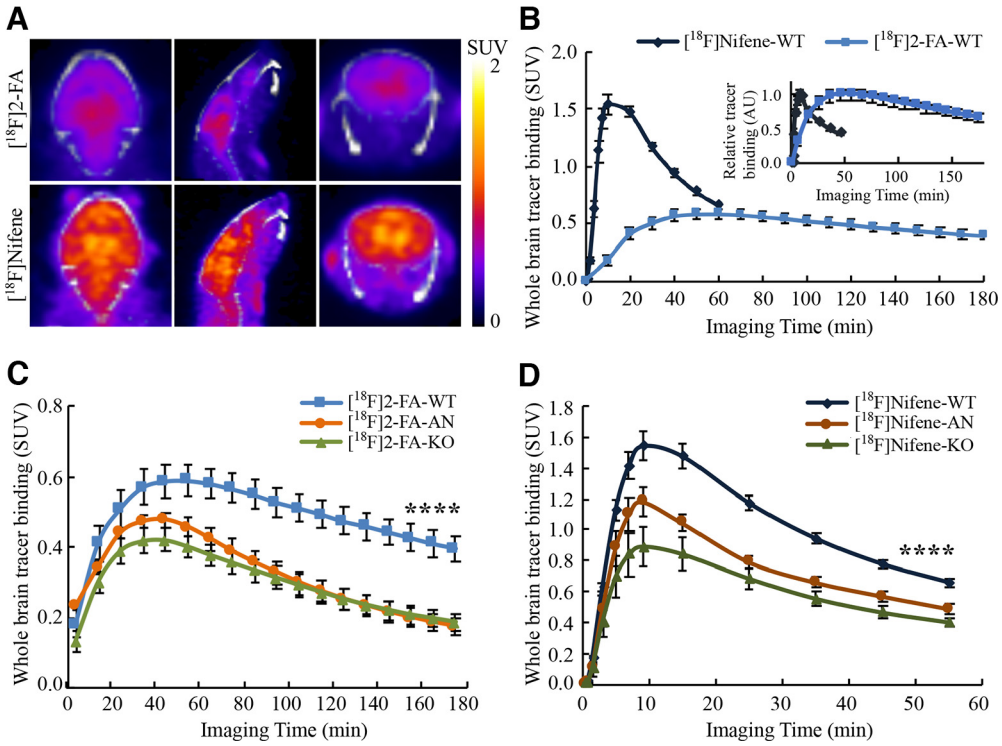

Figure 3. Binding and disassociation of [^{18}F]2-FA to $\alpha4\beta2$Rs is slower than [^{18}F]Nifene. ***A***, Brain images of [^{18}F]2-FA and [^{18}F]Nifene binding at coronal, sagittal, and transverse sections in WT mice. ***B***, Whole-brain TACs show [^{18}F]Nifene has faster binding kinetics compared with [^{18}F]2-FA. The insert compares both tracers after signal normalization to their highest binding, respectively. ***C***, ***D***, AN administration and $\beta2$-subunit KO diminish the binding of [^{18}F]2-FA & [^{18}F]Nifene.

also ~50% in the $\beta2$ KO mice compared with WT animals (Fig. 3*D*).

AN challenge in WT animals affected the whole-brain uptake and retention of both [^{18}F]2-FA and [^{18}F]Nifene similar to the decreases we observed with the $\beta2$ KO mice but to a lesser degree. The rapid addition of nicotine competes with both PET tracers resulting in fewer available $\alpha4\beta2$R binding sites and lower binding levels for the PET tracers. The initial higher uptake of both [^{18}F]2-FA and [^{18}F]Nifene compared with the KO mice is likely because of an inability of nicotine to occupy all available $\alpha4\beta2$R binding sites. In the case of [^{18}F]2-FA, AN brought the SUV levels at the end of the 3 h scan similar to the $\beta2$ KO mice brain (Fig. 3*C*). Retention of [^{18}F]Nifene after AN was similarly reduced with clearance profile similar to that found in the $\beta2$ KO mice brain (Fig. 3*D*).

[^{18}F]Nifene binding in brain regions

Regional brain distribution of [^{18}F]Nifene binding was analyzed in the thalamus, midbrain, hippocampus, striatum, cortex and cerebellum. In WT mice, [^{18}F]Nifene showed the highest SUV in the thalamus and midbrain and the lowest SUV in the cerebellum throughout the imaging duration (Fig. 4*A*). Time activity curves in the various regions followed a similar profile in all brain regions. Levels of [^{18}F]Nifene binding in the $\beta2$ KO mice brain were reduced to the level of cerebellum in all regions (Fig. 4*B*). In the case of AN administration initial levels of uptake were higher than $\beta2$ KO mice (Fig. 4*C*), which may be because of higher free fraction of [^{18}F]Nifene, but subsequently retention of [^{18}F]Nifene was not observed in receptor rich regions, unlike the WT without nicotine (Fig. 4*A*).

Figure 4*D* displays the TACs for CQWT mice, and compared with the WT mice (Fig. 4*A*), no difference in [^{18}F]Nifene uptake was noticed following CQ treatment. This is further illustrated by the SUV ratio to cerebellum curves for WT mice (Fig. 4*E*) and CQWT mice (Fig. 4*F*) showing similar levels of [^{18}F]Nifene-specific binding between groups.

Using the cerebellum as the reference region, DVR of [^{18}F]Nifene across all groups of mice are shown for the thalamus (Fig. 4*G*) and midbrain (Fig. 4*H*). The DVR values for $\beta2$ KO mice and AN-treated mice were <1. The WT mice had DVRs approaching 2 in the thalamus and over 1.6 in the midbrain. Differences between the WT and $\beta2$ KO mice were highly significant (adjusted $p < 0.0001$ for both thalamus and midbrain), as well as the difference between WT and AN-treated animals (adjusted $p < 0.0001$ for both thalamus and midbrain). The similar DVR levels of $\beta2$ KO mice and AN-treated animals confirms the apparent lack of receptor-mediated-specific binding. No significant difference was observed between [^{18}F]Nifene DVR in the WT and CQWT mice (adjusted $p > 0.05$), indicating that CQ treatment does not affect the binding of [^{18}F]Nifene *in vivo*, consistent with our observations *in vitro* (Fig. 1).

[^{18}F]2-FA binding in brain regions

In WT mice, [^{18}F]2-FA showed the highest SUV (~0.7) in the thalamus and midbrain and the lowest SUV in the cerebellum (~0.2–0.3) at the end of the imaging session (Fig. 5*A*). Other regions such as the striatum and cortex exhibited moderate levels of [^{18}F]2-FA binding. Compared with [^{18}F]Nifene (Fig. 4*A*), [^{18}F]2-FA SUVs did not reach a plateau within the 3-h scanning period. However, given that the residence time of varenicline in the brain is 4–5 d, the kinetics of [^{18}F]2-FA appear consistent to the slow kinetics of varenicline. All brain regions in the $\beta2$ KO mice exhibited a similar uptake and clearance profile with SUVs similar to cerebellum of ~0.2–0.3 (Fig. 5*B*). Similarly, AN was also able to block retention of [^{18}F]2-FA binding in various brain regions with SUVs similar to cerebellum of ~0.3 (Fig. 5*C*).

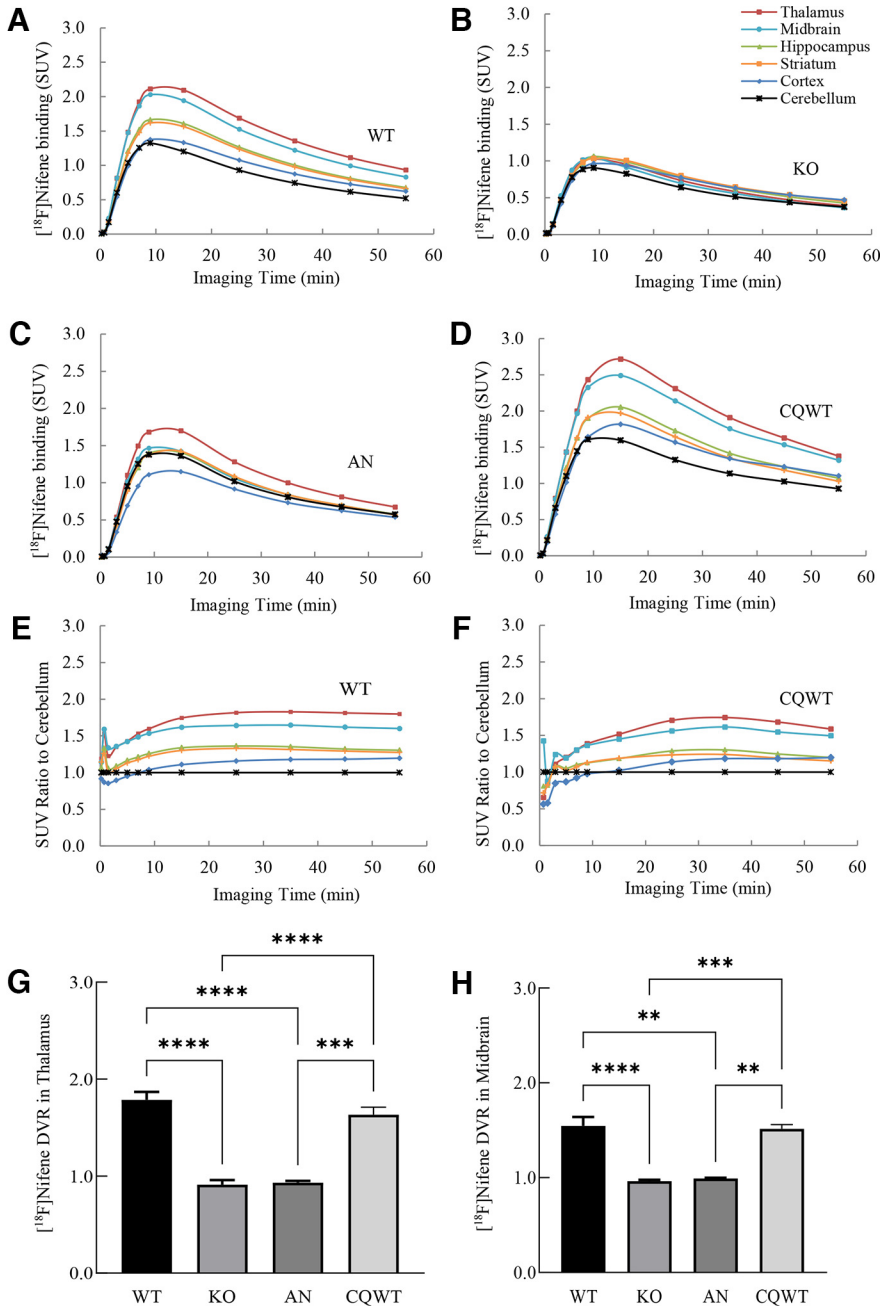

Figure 4. TACs of six brain regions shows that the thalamus and midbrain have the highest $\alpha4\beta2$R ligand binding while the cerebellum represents nonspecific binding. ***A***, TACs of [^{18}F]Nifene in six selected brain regions of WT mice. ***B***, TACs of [^{18}F]Nifene in KO mice. ***C***, TACs of [^{18}F]Nifene in AN mice. ***D***, TACs of [^{18}F]Nifene in CQ-treated WT mice. ***E***, ***F***, Binding ratios of each brain region to the cerebellum from WT mice and mice treated with CQ. ***G***, ***H***, Nifene DVR in the thalamus and midbrain of WT, KO, AN, and CQWT mice. KO and AN mice show reduced specific binding compared with WT mice. CQWT mice show no difference in DVR to WT mice.

Because the cerebellum had the lowest levels of [^{18}F]2-FA, DVR in other regions used the cerebellum as the reference region. The thalamus had the highest DVR (>2) in WT mice followed by the midbrain DVR (~2; Fig. 5*G*,*H*). The DVR values for $\beta2$ KO mice and AN-treated mice were <1. Differences between the WT and $\beta2$ KO mice were highly significant (adjusted $p < 0.0001$ for both thalamus and midbrain), as well as the difference between WT and AN-treated animals (adjusted $p < 0.0001$ for both thalamus and midbrain). The similar DVR levels of $\beta2$ KO mice and AN-treated animals confirms the apparent lack of receptor-mediated-specific binding.

To further test whether the mechanism causing [^{18}F]2-FA slow kinetics, mice were treated with CQ, which as discussed previously, dissipates the pH gradient across acidic organelles and reduced trapping *in vitro* (Fig. 1*D*; Govind et al., 2017). Previous studies had established that the maximum amount of CQ that can be injected into mice resulted in blood level of ~15 μM CQ for 3 d before PET imaging with [^{18}F]2-FA. Because of the reduced trapping of 2-FA observed *in vitro* following CQ treatment, we hypothesize that specific binding (i.e., DVR) of [^{18}F]2-FA *in vivo* will be significantly reduced and the tracer kinetics (i.e., washout) will be much faster compared with untreated WT mice. Decreases in DVR should be expected because administration of CQ, which reduces the GSat pH gradient, should displace [^{18}F]2-FA from the GSats, resulting in a higher concentration of free radiotracer. Increased uptake of [^{18}F]2-FA was observed in several brain regions after CQ treatment (Fig. 5*D*). This increase in [^{18}F]2-FA uptake may reflect an effect on the ability of [^{18}F]2-FA to sequester in intracellular acidic vesicles throughout the brain, which would increase levels of free [^{18}F]2-FA. Compared with the regional binding difference in WT mice (Fig. 5*A*), CQ reduced the regional differences of [^{18}F]2-FA binding although the nonspecific [^{18}F]2-FA binding increased in CQWT mice (Fig. 5*D*). This reduction in specific binding to $\alpha4\beta2$Rs and rapid washout of the tracer are more evident in the binding ratios of different regions to cerebellum (Fig. 5*E*,*F*). Total activity uptake of [^{18}F]2-FA in thalamus of the WT animals was ~2.5-fold over that in cerebellum at the end of 3-h imaging, while it was less than 1.5-fold in CQ-treated animals. Similarly, uptake of [^{18}F]2-FA in other brain regions were also reduced. The decrease in thalamic and midbrain DVR of CQ-treated mice were statistically significant (adjusted $p < 0.0001$ for both thalamus and midbrain; Fig. 5*G*,*H*). Thus, the results demonstrate that CQ treatment of the mice significantly reduced the specific [^{18}F]2-FA signal in the thalamus and midbrain consistent with it reducing 2-FA trapping as observed *in vitro* (Fig. 1*D*).

Discussion

Despite the known adverse consequences associated with smoking, smoking cessation is difficult. Even with the most effective smoking cessation reagent, varenicline, quitting rates reach only ~50% (Agboola et al., 2015). To rationally design better smoking cessation drugs, it is critical to understand the molecular and

cellular mechanisms governing how drugs dampen the effects of nicotine on the brain's reward pathway. Varenicline was designed as a high-affinity, partial agonist that mediates anti-smoking effects through acute, rapid interactions with $\alpha4\beta2$Rs that reduce the full-agonist effects of nicotine. Our lab has discovered additional long-term effects of varenicline in which varenicline is trapped in intracellular acidic vesicles and maintain brain levels throughout the day, importantly, after nicotine levels decline (Govind et al., 2017). We demonstrated that the slow release of trapped varenicline reduced the functionally upregulated $\alpha4\beta2$R currents, which should contribute to varenicline effects on smokers (Govind et al., 2017).

The "trapping hypothesis" has only been tested using *in vitro* systems. However, the long-term trapping of varenicline in GSats in the human brain explains why the rate of varenicline disposition is much slower (4–5 d) compared with that of untrapped and rapidly metabolized nicotine (1–2 h; Govind et al., 2017). Here, we extended our analysis *in vivo* using PET imaging in mice. Based on the differences in the kinetics during PET imaging, we predicted that the $\alpha4\beta2$R PET ligand, 2-FA with slow kinetics, is trapped in acidic vesicles similar to varenicline, and Nifene with much faster kinetics, would have significantly less trapping. ^{125}I-epibatidine binding *in vitro* to measure for reduction in $\alpha4\beta2$R upregulation as a measure of trapping confirmed that 2-FA is trapped in acidic vesicles similar to varenicline and Nifene displayed little trapping similar to nicotine (Fig. 1*C*).

We successfully employed both [^{18}F]2-FA and [^{18}F]Nifene in PET/CT mouse brain imaging of $\alpha4\beta2$Rs, making this study the first to use [^{18}F]2-FA in mouse models. As observed for studies in human and other animal models, the [^{18}F]2-FA uptake in the whole brain is much slower than that of [^{18}F]Nifene, peaking at ~50 versus ~10 min after the intraperitoneal tracer administration (Fig. 3*B–D*). This difference also holds true for the clearance of the two ligands from the brain (Fig. 3*B*). We observed statistically significant reduction of ligand binding in the whole brains of mice after AN injections and in the $\beta2$-subunit KO mice, demonstrating that most specific binding sites are found on $\beta2$-containing receptors.

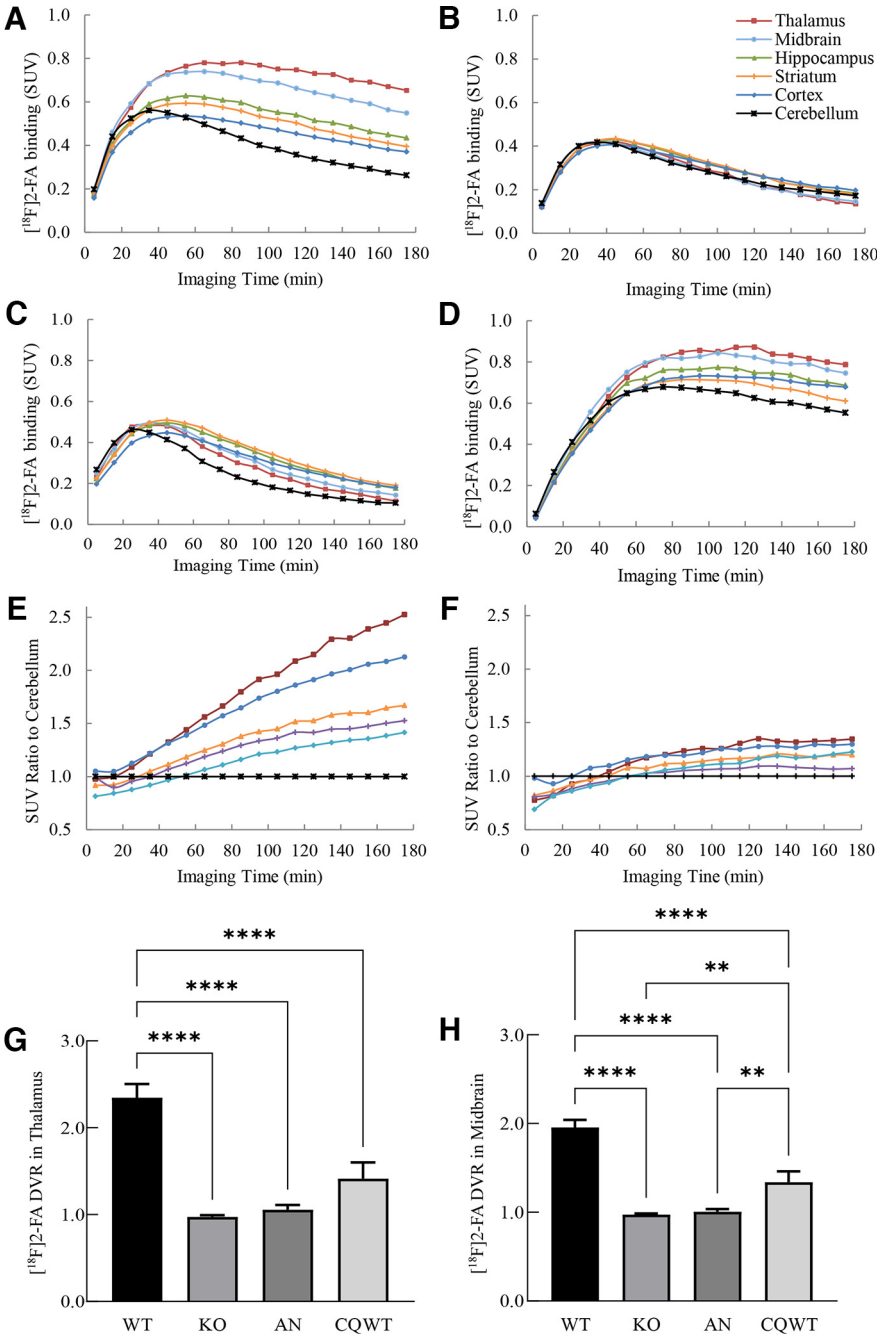

Figure 5. *In vivo* CQ treatment decreases the binding of [^{18}F]2-FA and slows its disassociation in six selected brain regions. ***A***, TACs of [^{18}F]2-FA in six selected brain regions from WT mice. ***B***, TACs of [^{18}F]2-FA in KO mice. ***C***, TACs of [^{18}F]2-FA in AN mice. ***D***, TACs of [^{18}F]2-FA in CQ-treated WT mice. ***E***, ***F***, Binding ratios of each brain region to the cerebellum from WT mice and mice treated with CQ. ***G***, ***H***, [^{18}F]2-FA DVR in the thalamus and midbrain of WT, KO, AN, and CQWT mice. KO, AN, and CQWT mice have reduced specific binding compared with WT mice.

Structural differences between 2-FA and Nifene can explain differences in the rates of entry into the brain and initial differences in binding levels (Fig. 3*B–D*). Both ligands have similar features: a 2-fluoropyridine group, a methoxyether linkage at the 3-position of the pyridine ring, and a secondary nitrogen in the 4-membered azetidine ring in 2-FA and 5-membered 3,4-dehydropyrrolidine ring in Nifene (Fig. 1*A*). However, the saturated 4-membered ring in 2-FA versus an unsaturated 5-membered ring in Nifene makes 2-FA more basic ($pK_a > 10$), while Nifene's unsaturated ring, which can delocalize electron density away from the nitrogen, is less basic (pK_a ~9). This difference in pK_a renders 2-FA more hydrophilic relative to Nifene. The lower lipophilicity and higher pK_a of 2-FA make it less permeable into the brain, because of a lower proportion of available uncharged species to cross the blood-brain barrier (BBB), whereas Nifene has a higher proportion of uncharged species which freely crosses into the brain. This difference in permeability is reflected in Figure 3*B–D* with a high initial

uptake of Nifene compared with 2-FA. The higher affinity of 2-FA and a high nonspecific binding component because of the higher pK_a also favors binding-rebinding of 2-FA at the receptor sites, further slowing down the dissociation kinetics. Nifene, with lower affinity and lower pK_a can more rapidly equilibrate and dissociate from the receptor sites, thus having a faster clearance rate.

Further analyses showed that two ligands displayed identical regional uptake with the highest uptake within the thalamus and midbrain (Fig. 3*A*), consistent with PET imaging studies in humans and other animal models (Hillmer et al., 2011, 2012, 2013; Mukherjee et al., 2018). Regional binding differences were diminished in AN mice and completely abolished in KO mice (Fig. 3*C*,*D*). These findings demonstrate that the ligand uptake in the cerebellum represents mostly nondisplaceable ligand signal. However, the WT mice displayed higher SUVs in the cerebellum compared with AN and KO mice for both [^{18}F]2-FA and [^{18}F]Nifene, indicating the presence of some ligand-specific binding. This cerebellum-specific binding signal is not unique to mice, as studies in rats using [^{18}F]2-FA PET found a nicotine displaceable signal component in this region (Vaupel et al., 2007). A study using [^{18}F]Nifene in rats also noticed significant ligand displacement in the cerebellum following administration of both lobeline and (-)nicotine, indicating the presence of specific binding (Hillmer et al., 2013). Because of the presence of this specific binding signal, DVR calculations using a cerebellum reference region will underestimate the binding potential. Because our study design takes advantage of AN and KO mice whose cerebellar-specific binding was completely abolished, only DVR values of the WT mice underestimate the true binding potential. Despite the underestimation, the WT mice displayed significantly higher DVR compared with all other groups, indicating that our choice of reference region was suitable for this application. The above-mentioned studies suggest the corpus collosum may be a suitable reference tissue for [^{18}F]2-FA and [^{18}F]Nifene PET studies. The corpus collosum was explored as a reference tissue for the current study, but displayed higher SUVs compared with the cerebellum in WT mice and displayed higher SUVs in WT mice compared with KO and AN mice. In addition, because of the small volume of the corpus collosum, the signal from this region was likely confounded by partial volume effects. Future studies should consider alternative reference regions or measurement of arterial blood for improved PET quantification.

CQ, which is a BBB permeable weak base and not a nicotinic ligand, has been used widely to reduce the pH gradient across intracellular acidic compartments. The decrease of the pH gradient across intracellular acidic vesicles has been directly measured in cultured cells (Dong et al., 2017). We found that inclusion of CQ in the medium at concentrations of 15–150 μM or NH_4Cl at 20 mM significantly reduced trapping of varenicline and 2-FA in cultured cells (Fig. 1*D*). We assume the reduction in trapping is caused by CQ entry in the $\alpha4\beta2$R-containing GSats vesicles reducing the pH gradient through their protonation without interfering with nicotinic ligand binding to $\alpha4\beta2$Rs so that weak base nicotinic ligand is less trapped. Comparing the [^{18}F]2-FA SUV TACs between the CQ mice and the untreated WT mice revealed that CQ resulted in uptake of the ligand in the target regions to more closely resemble the cerebellum (evident in Fig. 5*E*,*F*), indicating reduced specific binding in these regions and significantly faster [^{18}F]2-FA kinetics. Under the presence of CQ, regional brain uptake was higher than in the cerebellum, indicative of the presence of specific ligand binding. These results are consistent with [^{18}F]2-FA being trapped within intracellular acidic vesicles, the GSats, *in vivo* in the mouse brains. In contrast, CQ treatment before Nifene imaging did not result in changes of Nifene binding (Fig. 4*D*–*H*), suggesting that Nifene is not trapped in GSats *in vivo*.

Of interest is the use of dynamic PET data to measure the efflux rate of 2-FA from the acidic vesicles to compare with the *in vitro* findings. When generating the Logan plots, the tissue-to-plasma efflux rate (k_2') was determined using SRTM with a cerebellum reference tissue. For 2-FA, the efflux rate was determined as $0.033 \pm 0.0030\,min^{-1}$ (mean ± SEM). Compared with the efflux rate determined for Nifene ($0.45 \pm 0.084\,min^{-1}$), 2-FA reveals much slower washout from the brain. Future studies will explore measurement of the arterial blood curve and use of an image derived input function in different compartment models to estimate these rate constants, where the value of k_4 is likely to be a more accurate measure of the efflux of ligand from the intracellular acidic vesicles.

Taken together, our results are consistent with 2-FA and Nifene interacting with $\alpha4\beta2$Rs by different mechanisms. Because Nifene does not get trapped significantly in the $\alpha4\beta2$R-containing GSats, its exit from neurons expressing $\alpha4\beta2$Rs is only delayed by the binding and unbinding to the receptors and is a measure of the total $\alpha4\beta2$R population, both cell-surface and in intracellular receptors. 2-FA binds to $\alpha4\beta2$Rs in the GSats and becomes trapped for many hours. Because its binding and unbinding to receptors outside the GSats is so much faster than its exit rate from the GSats, its PET signal in the brain is a measure of only GSats pools of receptors. In short, the two ligands measure separate $\alpha4\beta2$R features.

In this study, we have combined *in vitro* cellular assays with *in vivo* PET and new insights into the changes that occur during nicotine addiction have emerged that could help design more effective anti-smoking drugs. Specifically, our findings suggest that design elements, such as pK_a and receptor affinity that regulate trapping in the GSats, need to be explored in terms of drug design. The same drug design strategy can be applied to other neurologic conditions in which nicotinic receptors are implicated such as dementia (Picciotto et al., 2002), depression (Picciotto et al., 2002), and attention deficits (Faraone and Biederman, 1998).

References

Agboola SA, Coleman T, McNeill A, Leonardi-Bee J (2015) Abstinence and relapse among smokers who use varenicline in a quit attempt-a pooled analysis of randomized controlled trials. Addiction 110:1182–1193.

Albuquerque EX, Pereira EF, Alkondon M, Rogers SW (2009) Mammalian nicotinic acetylcholine receptors: from structure to function. Physiol Rev 89:73–120.

Benwell ME, Balfour DJ, Anderson JM (1988) Evidence that tobacco smoking increases the density of (-)-[3H]nicotine binding sites in human brain. J Neurochem 50:1243–1247.

Bieszczad KM, Kant R, Constantinescu CC, Pandey SK, Kawai HD, Metherate R, Weinberger NM, Mukherjee J (2012) Nicotinic acetylcholine receptors in rat forebrain that bind ^{18}F-nifene: relating PET imaging, autoradiography, and behavior. Synapse 66:418–434.

Breese CR, Adams C, Logel J, Drebing C, Rollins Y, Barnhart M, Sullivan B, Demasters BK, Freedman R, Leonard S (1997) Comparison of the regional expression of nicotinic acetylcholine receptor alpha7 mRNA and [125I]-alpha-bungarotoxin binding in human postmortem brain. J Comp Neurol 387:385–398.

Brown DA, Garthwaite J (1979) Intracellular pH and the distribution of weak acids and bases in isolated rat superior cervical ganglia. J Physiol 297:597–620.

Brown L, Chefer S, Pavlova O, Vaupel DB, Koren AO, Kimes AS, Horti AG, Mukhin AG (2004) Evaluation of 5-(2-(4-pyridinyl)vinyl)-6-chloro-3-(1-methyl-2-(S)-pyrrolidinylmethoxy)pyridine and its analogues as PET radioligands for imaging nicotinic acetylcholine receptors. J Neurochem 91:600–612.

Chattopadhyay S, Xue B, Collins D, Pichika R, Bagnera R, Leslie FM, Christian BT, Shi B, Narayanan TK, Potkin SG, Mukherjee J (2005) Synthesis and evaluation of nicotine alpha4beta2 receptor radioligand, 5-(3'-18F-fluoropropyl)-3-(2-(S)-pyrrolidinylmethoxy)pyridine, in rodents and PET in nonhuman primate. J Nucl Med 46:130–140.

Constantinescu CC, Garcia A, Mirbolooki MR, Pan ML, Mukherjee J (2013) Evaluation of [18F]Nifene biodistribution and dosimetry based on whole-body PET imaging of mice. Nucl Med Biol 40:289–294.

Davila-Garcia MI, Musachio JL, Perry DC, Xiao Y, Horti A, London ED, Dannals RF, Kellar KJ (1997) [125I]IPH, an epibatidine analog, binds with high affinity to neuronal nicotinic cholinergic receptors. J Pharmacol Exp Ther 282:445–451.

Dong B, Song X, Kong X, Wang C, Zhang N, Lin W (2017) A tumor-targeting and lysosome-specific two-photon fluorescent probe for imaging pH changes in living cells. J Mater Chem B 5:988–995.

Faraone SV, Biederman J (1998) Neurobiology of attention-deficit hyperactivity disorder. Biol Psychiatry 44:951–958.

Gao Y, Kuwabara H, Spivak CE, Xiao Y, Kellar K, Ravert HT, Kumar A, Alexander M, Hilton J, Wong DF, Dannals RF, Horti AG (2008) Discovery of (-)-7-methyl-2-exo-[3'-(6-[18F]fluoropyridin-2-yl)-5'-pyridinyl]-7-azabicyclo[2.2.1]heptane, a radiolabeled antagonist for cerebral nicotinic acetylcholine receptor (alpha4beta2-nAChR) with optimal positron emission tomography imaging properties. J Med Chem 51:4751–4764.

Govind AP, Vezina P, Green WN (2009) Nicotine-induced upregulation of nicotinic receptors: underlying mechanisms and relevance to nicotine addiction. Biochem Pharmacol 78:756–765.

Govind AP, Walsh H, Green WN (2012) Nicotine-induced upregulation of native neuronal nicotinic receptors is caused by multiple mechanisms. J Neurosci 32:2227–2238.

Govind AP, Vallejo YF, Stolz JR, Yan JZ, Swanson GT, Green WN (2017) Selective and regulated trapping of nicotinic receptor weak base ligands and relevance to smoking cessation. Elife 6:e25651.

Govind AP, Jeyifous O, Russell TA, Yi Z, Weigel AV, Ramaprasad A, Newell L, Ramos W, Valbuena FM, Casler JC, Yan JZ, Glick BS, Swanson GT, Lippincott-Schwartz J, Green WN (2021) Activity-dependent Golgi satellite formation in dendrites reshapes the neuronal surface glycoproteome. Elife 10:e68910.

Hansch C, Leo A (1995) Exploring QSAR: volume 1: fundamentals and applications in chemistry and biology. Washington, DC: American Chemical Society.

Hesterman J, Ghayoor A, Novicki A, Wang X, Cadoret Y, Becerra L, Gunn R, Avants B (2019) Multi-atlas approaches for image segmentation across modality, species and application area. Konica Minolta Technol Rep 16:32–36.

Hillmer AT, Wooten DW, Moirano JM, Slesarev M, Barnhart TE, Engle JW, Nickles RJ, Murali D, Schneider ML, Mukherjee J, Christian BT (2011) Specific $\alpha4\beta2$ nicotinic acetylcholine receptor binding of [F-18]nifene in the rhesus monkey. Synapse 65:1309–1318.

Hillmer AT, Wooten DW, Slesarev MS, Ahlers EO, Barnhart TE, Murali D, Schneider ML, Mukherjee J, Christian BT (2012) PET imaging of $\alpha4\beta2^*$ nicotinic acetylcholine receptors: quantitative analysis of 18F-nifene kinetics in the nonhuman primate. J Nucl Med 53:1471–1480.

Hillmer AT, Wooten DW, Farhoud M, Barnhart TE, Mukherjee J, Christian BT (2013) The effects of lobeline on $\alpha4\beta2^*$ nicotinic acetylcholine receptor binding and uptake of [(18)F]nifene in rats. J Neurosci Methods 214:163–169.

Horti AG, Chefer SI, Mukhin AG, Koren AO, Gündisch D, Links JM, Kurian V, Dannals RF, London ED (2000) 6-[18F]fluoro-A-85380, a novel radioligand for in vivo imaging of central nicotinic acetylcholine receptors. Life Sci 67:463–469.

Huang SC (2000) Anatomy of SUV. Standardized uptake value. Nucl Med Biol 27:643–646.

Karlin A (2002) Emerging structure of the nicotinic acetylcholine receptors. Nat Rev Neurosci 3:102–114.

Keyes JW (1995) SUV: standard uptake or silly useless value? J Nucl Med 36:1836–1839.

Krishnamoorthy S, Blankemeyer E, Mollet P, Surti S, Van Holen R, Karp JS (2018) Performance evaluation of the MOLECUBES β-CUBE-a high spatial resolution and high sensitivity small animal PET scanner utilizing monolithic LYSO scintillation detectors. Phys Med Biol 63:155013.

Lewis AS, Picciotto MR (2013) High-affinity nicotinic acetylcholine receptor expression and trafficking abnormalities in psychiatric illness. Psychopharmacology (Berl) 229:477–485.

Logan J, Fowler JS, Volkow ND, Wang GJ, Ding YS, Alexoff DL (1996) Distribution volume ratios without blood sampling from graphical analysis of PET data. J Cereb Blood Flow Metab 16:834–840.

Lu H, Chen X, Zhan CG (2007) First-principles calculation of pKa for cocaine, nicotine, neurotransmitters, and anilines in aqueous solution. J Phys Chem B 111:10599–10605.

Marks MJ, Burch JB, Collins AC (1983) Effects of chronic nicotine infusion on tolerance development and nicotinic receptors. J Pharmacol Exp Ther 226:817–825.

Marubio LM, Gardier AM, Durier S, David D, Klink R, Arroyo-Jimenez MM, McIntosh JM, Rossi F, Champtiaux N, Zoli M, Changeux JP (2003) Effects of nicotine in the dopaminergic system of mice lacking the alpha4 subunit of neuronal nicotinic acetylcholine receptors. Eur J Neurosci 17:1329–1337.

Maskos U, Molles BE, Pons S, Besson M, Guiard BP, Guilloux JP, Evrard A, Cazala P, Cormier A, Mameli-Engvall M, Dufour N, Cloëz-Tayarani I, Bemelmans AP, Mallet J, Gardier AM, David V, Faure P, Granon S, Changeux JP (2005) Nicotine reinforcement and cognition restored by targeted expression of nicotinic receptors. Nature 436:103–107.

Mazur C, et al. (2019) Brain pharmacology of intrathecal antisense oligonucleotides revealed through multimodal imaging. JCI Insight 4:e129240.

Mukherjee J, Lao PJ, Betthauser TJ, Samra GK, Pan ML, Patel IH, Liang C, Metherate R, Christian BT (2018) Human brain imaging of nicotinic acetylcholine $\alpha4\beta2^*$ receptors using [^{18}F]Nifene: selectivity, functional activity, toxicity, aging effects, gender effects, and extrathalamic pathways. J Comp Neurol 526:80–95.

National Center for Chronic Disease Prevention and Health Promotion (US) Office on Smoking and Health (2014) The health consequences of smoking—50 years of progress: a report of the surgeon general. Atlanta: Centers for Disease Control and Prevention (US).

Picciotto MR, Zoli M, Léna C, Bessis A, Lallemand Y, Le Novère N, Vincent P, Pich EM, BrÃlet P, Changeux JP (1995) Abnormal avoidance learning in mice lacking functional high-affinity nicotine receptor in the brain. Nature 374:65–67.

Picciotto MR, Zoli M, Rimondini R, Léna C, Marubio LM, Pich EM, Fuxe K, Changeux JP (1998) Acetylcholine receptors containing the beta2 subunit are involved in the reinforcing properties of nicotine. Nature 391:173–177.

Picciotto MR, Brunzell DH, Caldarone BJ (2002) Effect of nicotine and nicotinic receptors on anxiety and depression. Neuroreport 13:1097–1106.

Pichika R, Easwaramoorthy B, Collins D, Christian BT, Shi B, Narayanan TK, Potkin SG, Mukherjee J (2006) Nicotinic alpha4-beta2 receptor imaging agents: part II. Synthesis and biological evaluation of 2-[18F]fluoro-3-[2-((S)-3-pyrrolinyl)methoxy]pyridine (18F-nifene) in rodents and imaging by PET in nonhuman primate. Nucl Med Biol 33:295–304.

Sallette J, Pons S, Devillers-Thiery A, Soudant M, Prado de Carvalho L, Changeux JP, Corringer PJ (2005) Nicotine upregulates its own receptors through enhanced intracellular maturation. Neuron 46:595–607.

Samra GK, Intskirveli I, Govind AP, Liang C, Lazar R, Green WN, Metherate R, Mukherjee J (2018) Development of fluorescence imaging probes for nicotinic acetylcholine $\alpha4\beta2$. Bioorg Med Chem Lett 28:371–377.

Schwartz RD, Kellar KJ (1983) Nicotinic cholinergic receptor binding sites in the brain: regulation in vivo. Science 220:214–216.

Slavine NV, Kulkarni PV, McColl RW (2017) Iterative image processing for early diagnostic of beta-amyloid plaque deposition in preclinical Alzheimer's disease studies. J Appl Bioinforma Comput Biol 6:134.

Thompson AJ, Metzger S, Lochner M, Ruepp MD (2017) The binding orientation of epibatidine at α7 nACh receptors. Neuropharmacology 116:421–428.

Valette H, Bottlaender M, Dolle F, Guenther I, Fuseau C, Coulon C, Ottaviani M, Crouzel C (1999) Imaging central nicotinic acetylcholine receptors in baboons with [18F]fluoro-A-85380. J Nucl Med 40:1374–1380.

Vallejo YF, Buisson B, Bertrand D, Green WN (2005) Chronic nicotine exposure upregulates nicotinic receptors by a novel mechanism. J Neurosci 25:5563–5572.

Vaupel DB, Stein EA, Mukhin AG (2007) Quantification of alpha4beta2* nicotinic receptors in the rat brain with microPET and 2-[18F]F-A-85380. Neuroimage 34:1352–1362.

Vezina P, McGehee DS, Green WN (2007) Exposure to nicotine and sensitization of nicotine-induced behaviors. Prog Neuropsychopharmacol Biol Psychiatry 31:1625–1638.

Vodicka P, Lim J, Williams DT, Kegel KB, Chase K, Park H, Marchionini D, Wilkinson S, Mead T, Birch H, Yates D, Lyons K, Dominguez C, Beconi M, Yue Z, Aronin N, DiFiglia M (2014) Assessment of chloroquine treatment for modulating autophagy flux in brain of WT and HD mice. J Huntingtons Dis 3:159–174.

Walsh RM, Roh SH, Gharpure A, Morales-Perez CL, Teng J, Hibbs RE (2018) Structural principles of distinct assemblies of the human $\alpha4\beta2$ nicotinic receptor. Nature 557:261–265.